Strong coupling and exceptional points in optically pumped active hyperbolic metamaterials

Fabio Vaianella,*,† Joachim M. Hamm,‡ Ortwin Hess,‡ and Bjorn Maes†

†*Micro- and Nanophotonic Materials Group, Faculty of Science, University of Mons, 20, place du Parc, B-7000 Mons, Belgium*

‡*The Blackett Laboratory, Department of Physics, Imperial College London, South Kensington Campus, London SW7 2AZ, UK*

E-mail: Fabio.Vaianella@umons.ac.be

Abstract

We investigate the interaction of light in gain-enhanced multilayered hyperbolic metamaterials in the strong interaction regime. Pumping the dye in the dielectric layers from inside the light cone, while emission occurs into the lower hyperbolic band outside the light cone, eases the problem of light incoupling. In the strong coupling regime both emission and absorption lines cause a distortion of the plasmonic modes due to Rabi splitting and a $\mathcal{PT}$-symmetry broken phase, with generation of exceptional points at loss-gain compensation frequencies. We derive a semi-classical model that describes these phenomena for finite and infinite devices in detail, requiring only the overlap factor and the complex frequencies of the dye transition and the optical mode.

Keywords

hyperbolic metamaterials, active plasmonics, strong coupling, exceptional points

In the last decades metamaterials have attracted tremendous scientific interest owing to their abilities to manipulate electromagnetic waves in manners not found in nature[1–3]. Driven by recent advances in nanolithography and nanochemistry new types of functionalized optical metamaterials have emerged, profiting from a strongly enhanced interaction with inclusions of nonlinear and gain materials on subwavelength scales[4–8]. In particular, valuable opportunities are offered by hyperbolic metamaterials (HMMs), which typically consist of periodic stacks of metallic and dielectric layers or arrays of metallic nanorods inside a dielectric host[9]. It is the combination of structural simplicity[10–12] with a range of interesting properties (such as negative refraction[13], an extremely large optical density of states[14–16], large propagation constants[17], subwavelength imaging far below the diffraction limit[18,19]) that makes these metamaterials ideal candidates for a range of applications, such as lithography[20,21] and sensing[22]. However, like many metamaterials based on metal-dielectric structures, HMMs often suffer from high ohmic losses[23–25]. The inclusion of gain media in the dielectric material offers a pathway to mitigate these losses[26–32], and gives rise to the new class of active HMMs, where light strongly interacts with quantum transitions of the active medium[33–36].

Here, we investigate a multilayer HMM structure infiltrated with dye molecules inside the dielectric layers, which can conveniently be modelled on the basis of a four-level (quantum) system. While the weak coupling regime was studied for loss-compensation[37], we here consider strong coupling with large oscillator strengths, where light enters a dressed state with electronic transitions associated with both the absorption and the emission line of the dye[38–40]. Previously, Shekhar and Jacob[41] theoretically investigated strong coupling between the intersubband absorption line of a multiple quantum-well gain medium and the bulk polariton of a finite HMM. However, the simultaneous interaction of light with an absorption and an emission line, as present in optically pumped gain media such as dyes, has to the

best of our knowledge not been studied yet.

The proposed HMM is fundamentally simple to fabricate and features a bandstructure optimized for efficient incoupling from within the light cone. It also exhibits rich physics that ties multiple concepts together, as exposed by detailed analytical and numerical modeling. The absorption line of the dye leads to strong coupling features, with large momentum modes exhibiting the typical avoided crossings via Rabi splitting. On the other hand, the gain provided gives rise to exceptional points (EPs) close to the emission line, which are actively examined in parity-time ($\mathcal{PT}$) symmetry studies[42,43]. We show that these EPs lead to group velocity singularities and arise naturally when the band edges intersect with the inversion line, i.e., where the losses are precisely compensated by gain. Thus the four-level dye brings various related features together in a judiciously tailorable fashion. Both the finite and the infinite multilayers are discussed, each time showing the same class of effects, but in a particularly distinctive way. An important result is our semi-analytical theory, which faithfully models and explains the behaviors of the modes at play, and matches very well with exact transfer-matrix calculations.

In section 1 we detail the structure, together with the dye parameters, and analyze the passive dispersion diagram. The theory for passive and optically pumped active HMMs is presented in section 2, including a semi-analytical model for coupling with the electronic dye transitions. In the results section 3 we first discuss the interaction of finite and infinite HMMs with absorption or emission lines in isolation, and then with the full four-level dye model.

1 Structure

As a practical realization of an optically pumped HMM we propose a multilayer structure where dye-infiltrated epoxy is spin-coated on silver layers[44], represented in Figure 1a (period delimited by the orange dashed lines). The dye that provides gain is represented by a four-

level model, with energy levels as sketched in Figure 1b. Pumping of the dye and population inversion involves the excitation of electrons from the fundamental level with energy E_1 to the excited state E_2 (blue arrow in Figure 1b). The electrons relax through fast non-radiative processes (green arrows in Figure 1b) and spontaneous and stimulated light emission occurs via the optically active transition from E_3 to E_4 providing gain (red arrow in Figure 1b).

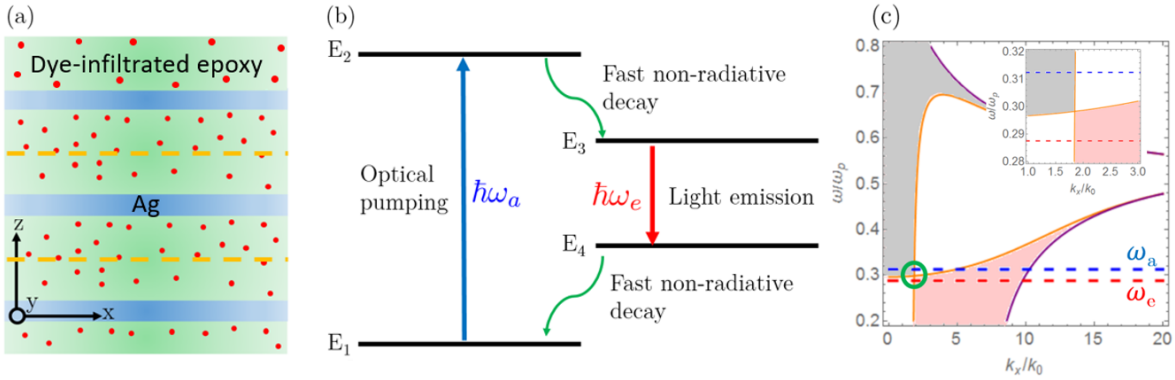

Figure 1: (a) Schematic of the active HMM, consisting of silver (blue) and dye infiltrated (red dots) epoxy layers (green), with a unit cell marked by orange dashed lines. (b) Energy diagram of a four-level dye molecule, with an absorption (blue) and emission line (red). (c) Illustration of the plasmonic bands of the passive HMM with the dye absorption line at frequency ω_a (blue dashed line) above and the emission line at frequency ω_e (red dashed line) below the intersection point, highlighted by the green circle, where the upper (grey shaded) and lower band (red shaded) connect. Inset of (c) shows a zoom on this intersection point.

Further, to accommodate for optical pumping and solve the problem of light-injection into hyperbolic modes literally on the fly, we propose a structure where high-energy pump light can propagate inside the structure to excite the dye, providing gain at the lower emission frequency. A typical dispersion of a hyperbolic multilayer is depicted in Figure 1c, where the orange curves are the dispersions at the center of the Brillouin zone and the purple curves at the edge of the Brillouin zone (see below for more details). The multilayer presents thus two distinct plasmonic bands, the lower one providing the propagation of extremely high momentum waves (red shaded zone in Figure 1c), and the upper one lying partially inside the light cone (grey shaded zone in Figure 1c). For this reason it is crucial that the absorption line of the dye falls within the upper band inside the light cone, while the

emission line resides in the lower band (horizontal dashed lines in Figure 1c). This particular arrangement allows for light emission into the hyperbolic modes, benefiting simultaneously from both a strong field enhancement and large wavevectors.

2 Theory

In this section we start with a standard theory of passive HMMs, then we motivate our choice of parameters for the dye-infiltrated structure, and subsequently we develop a semi-analytical model that describes optical mode coupling with the dye transitions.

Passive HMMs. Effective medium theory is often used to approximately describe the optical properties of hyperbolic multilayers[45–47]. However, as pointed out, the effective medium model becomes increasingly inaccurate for larger wavevectors and frequencies, as the quasi-static approximation breaks down[48–50].

Rather than relying on the effective medium approximation, we use the exact dispersion relation (for TM polarization), which is found directly by solving Bloch's eigenvalue equation $M\mathbf{b} = \lambda_{\pm}\mathbf{b}$, where M is the transfer matrix of the unit cell, and $\mathbf{b}$ the Bloch eigenvectors. The Bloch eigenvalues can be represented as $\lambda_{\pm} = e^{\pm ik_z D}$ where $D = d_m + d_d$ is the thickness of the unit cell, and k_z the Bloch wavevector. The exact dispersion for a two-layer metal-dielectric HMM is[51,52]

$$\begin{aligned}\Lambda = \cos(k_z D) = &\frac{(\kappa_d\varepsilon_m + \kappa_m\varepsilon_d)^2}{4\kappa_d\kappa_m\varepsilon_d\varepsilon_m}\cosh(\kappa_d d_d + \kappa_m d_m)\\ &- \frac{(\kappa_d\varepsilon_m - \kappa_m\varepsilon_d)^2}{4\kappa_d\kappa_m\varepsilon_d\varepsilon_m}\cosh(\kappa_d d_d - \kappa_m d_m)\end{aligned} \tag{1}$$

with decay coefficients $\kappa_{d,m} = (k_x^2 - k_0^2\varepsilon_{d,m})^{1/2}$ in the dielectric and metallic layers, respectively. In this work a simple Drude model, $\varepsilon_m = 1 - \omega_p^2/(\omega^2 + i\omega\gamma_p)$, with plasma frequency $\omega_p = 1.26 \times 10^{16}\,\mathrm{rad/s}$ and damping rate $\gamma_p = 5 \times 10^{13}\,\mathrm{s}^{-1}$ is used to model the silver layers

in the visible regime[53–55]. Using Eq. 1 we can express the Bloch eigenvalues as

$$\lambda_{\pm} = \cos(k_z D) \pm i \sin(k_z D) = \Lambda \pm i\sqrt{1-\Lambda^2}\,. \tag{2}$$

Thus, the eigenvalues become degenerate when $\Lambda = \pm 1$, which implies $\mathrm{Re}(\Lambda) = \pm 1$ and $\mathrm{Im}(\Lambda) = 0$, i.e., when $k_z D$ is purely real and the Bloch wavector is at the center or edges of the Brillouin zone (where $k_z = 0$ or $k_z = \pi/D$ so $\cos(k_z D) = \pm 1$). This statement remains valid for active multilayer structures and implies the existence of exceptional points at the intersection of the loss-compensation curves (defined by the $\mathrm{Im}(\Lambda) = 0$ condition) and the edges of the plasmonic bands (more details later in the Results section).

As explained in the previous section, the intersection point between the upper and lower bands of the HMM (highlighted by the green circle in Figure 1c) is of particular interest for the design of the active, optically pumped HMM, and the geometric and dye parameters should be selected carefully. This intersection point has the frequency[51]

$$\omega_i = \frac{\omega_p}{\sqrt{1+\varepsilon_d(d_d/d_m)}}. \tag{3}$$

To facilitate pumping into the upper band and emission into the lower band (horizontal lines in Figure 1c), the layer thicknesses need to be chosen such that for the given dye the peaks of absorption and emission lines fall above and below the intersection point, respectively.

Dye-Infiltrated Multilayer. To demonstrate the feasibility of optical pumping in the structure, we consider realistic material parameters for the dye model. Rhodamine 6G, frequently used for loss-compensation in optical metamaterials[56,57], has peak emission and absorption wavelengths at 520 nm and 480 nm, which translates into angular frequencies $\omega_e = 0.288\,\omega_p$ and $\omega_a = 0.313\,\omega_p$. The respective linewidths are approximately $\gamma_{e,a} = 0.005\,\omega_p$. With the dye embedded in epoxy ($\varepsilon_{\mathrm{epoxy}} = 2.56$) the permittivity of the active dielectric

layers is modeled by Lorentzians (see Supporting Information for more details)

$$\varepsilon_d = 2.56 + g_a L(\omega_a, \gamma_a) + g_e L(\omega_e, \gamma_e) \tag{4}$$

where

$$L(\omega_j, \gamma_j) = -\frac{2}{\pi} \frac{\omega_j}{(\omega^2 - \omega_j^2 - \gamma_j^2) + 2i\gamma_j} \tag{5}$$

is the normalized second-order Lorentzian line-shape function of the excitonic transitions. The coupling strengths g_a and g_e determine the oscillator strength of the absorption and emission lines, respectively. While they generally depend on the population of the various levels (Figure 1b), we here assume an inverted system with equal coupling strengths but opposite signs, $g_e = -g_a$ (where $g_a > 0$), for the emission and absorption lines.

To push the absorption line into the upper and the emission line into the lower band (Figure 1c) we align the intersection point (green circle in Figure1c) between the two transitions at $\omega = 0.3\,\omega_p$. From Eq. 3 we thus find the required ratio of layer thicknesses $d_d \approx 4\,d_m$. In addition, to allow for large wavevectors, which are useful for instance for imaging applications, we aim for a large bandwidth of the lower band. The period therefore needs to be as small as possible, as the wavevector along z is limited by the Brillouin zone edge ($|k_{z,max}| = \pi/D$). Considering fabrication constraints we choose $d_m = 5\,\text{nm}$, as vapor deposited silver layers of this thickness are sufficiently smooth when a 1 nm thick germanium layer is used as a wetting layer[44,58], and $d_d = 20\,\text{nm}$, which is readily achievable by spin-coating.

To determine the effectiveness of the optical pump scheme, we first calculate the light transmittance of the passive multilayer for a finite structure of 10 periods. Figure 2a shows that transmission of incident waves above $\omega = 0.3\,\omega_p$ from inside the light cone is almost perfect (white region). Note that, for finite multilayers the plasmonic bands are replaced by discrete modes, as opposed to the continuous bands observed for infinite structures. A typical eigenmode profile is presented in Figure 2b, showing the magnetic field profile of the

third discrete eigenmode of the lower band at $\omega = 0.25\,\omega_p$ (marked by a black star in Figure 2a). This mode is symmetric and presents three maximas and two nodes. When the order of the mode increases, the number of nodes increases and the interaction with the gain medium is then reduced.

As the passive structure is almost transparent to the pump, absorption of light by the dyes should be effective. To confirm this we calculate (with the commercial finite-element software COMSOL Multiphysics 5.2) the absorbance within the various layers with dyes for normal incidence ($k_x = 0$), by taking into account the absorption line only (emission switched off), see Figure 2c. The total absorbance by the dyes (blue curve) at the central absorption frequency is almost 90%, with about 25% of the light absorbed in the first period (brown curve), and 10% in the fifth period (yellow curve). For the last period (purple curve) the absorbance is small as most of the light has already been absorbed. We note that with the population numbers fixed, this analysis neglects saturation effects, which render the dielectric layers transparent with increasing pump strength, until all layers are equally pumped into inversion.

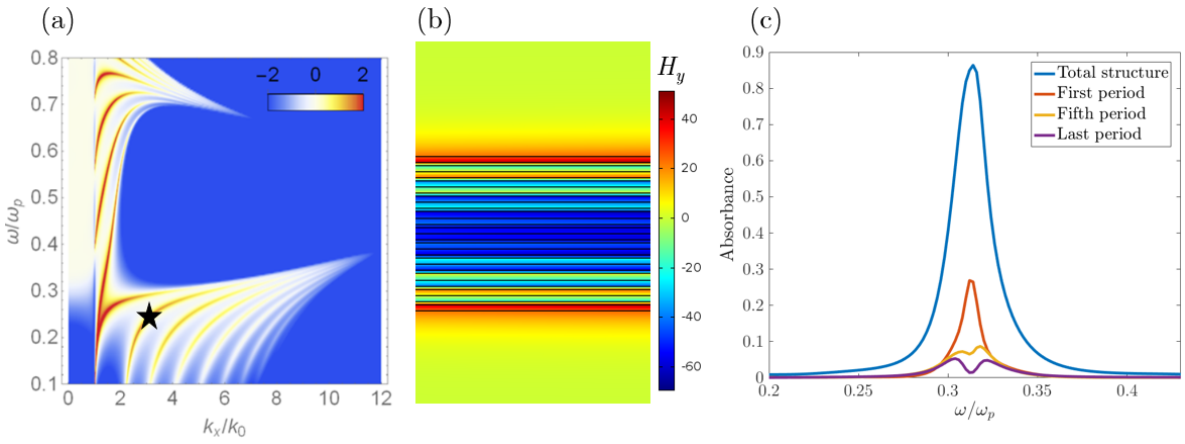

Figure 2: (a) Transmittance of a finite HMM of 10 periods with thickness $d_m = 5\,\text{nm}$ (logarithmic scale). (b) Magnetic field profile H_y of the third eigenmode of the lower band at $\omega = 0.25\,\omega_p$, marked by a black star in Figure 2a. (c) Absorbance at normal incidence ($\omega_a = 0.313\,\omega_p$) of the dyes for the whole structure (blue curve), the first period (brown curve), the fifth period (yellow curve) and the last period (purple curve), respectively.

Semi-Classical Model. To understand the coupling of the modes with the dyes, we

develop a model that describes the behavior of the oscillators. As the four-level dye presents an absorption and an emission line, with opposite signs for the coupling strength, we expect to have two distinct interactions at these frequencies.

For finite structures (Figure 2a) the continuous bands are replaced by discrete resonant modes, with the number of these modes per band equal to the number of periods (there are 10 modes for a 10-period stack, note that some of the modes are invisible with the scale of Figure 2a). When infiltrated with dyes, coupling between these discrete modes and the excitonic lines occurs. For simplicity, we first examine coupling with only one excitonic line (either the emission or absorption line) before showing the full model. From the Maxwell-Bloch equations and the wave equation we derive a semi-classical model for this system, which results in coupled oscillator equations for the modal field amplitude E and the polarization of the respective transition P (see details in Supporting Information):

$$\partial_t \begin{pmatrix} E \\ P/\varepsilon_0 \end{pmatrix} = -i\Omega_{\pm} \begin{pmatrix} E \\ P/\varepsilon_0 \end{pmatrix} = \begin{pmatrix} -i\Omega_m & iA_m \\ iK_{12} & -i\Omega_{12} \end{pmatrix} \begin{pmatrix} E \\ P/\varepsilon_0 \end{pmatrix}, \tag{6}$$

where Ω_m and Ω_{12} are the complex frequencies of the selected optical mode and the excitonic transition (absorption or emission), whose negative imaginary parts are the modal damping rate γ_m and the linewidth of the transition (γ_a or γ_e), respectively. The off-diagonal coupling terms are determined as $A_m = \Omega_m\Gamma/2$ and $K_{12} = \sigma_{12}/\varepsilon_0$, introducing the spatial overlap factor Γ of the plasmonic mode with the dielectric medium, and the cross-section σ_{12} of the excitonic transition under consideration. The latter relates to the coupling strength of the oscillator via $g = \pi\sigma_{12}/\varepsilon_0$.

Solving for the eigenfrequencies $\Omega_{\pm}$ of the coupled system we find

$$\Omega_{\pm} = \frac{1}{2}(\Omega_m + \Omega_{12}) \pm \frac{1}{2}\sqrt{4K_{12}A_m + (\Omega_m - \Omega_{12})^2}, \tag{7}$$

which defines the mode splitting within the semi-classical coupling model for two oscillators.

Note that, with all other parameters determined, the only remaining parameters to fit are the frequency of the selected optical mode Ω_m, and its spatial overlap factor Γ with the gain layers. Both parameters only depend on properties of the passive structure and are independent of the dye characteristics. For the given structure we determine $\gamma_m \approx 0.004\,\omega_p$ for the decay rate of the modes (γ_m does not change much for the various modes of the lower band) and an overlap factor of $\Gamma \approx 1/3$ as best fits to the modes shown in Figure 2a. Both parameters prove to be relatively frequency insensitive within the range under consideration (between 0.2 and 0.4 ω_p).

Unlike the standard classical oscillator model, the semi-classical model predicts different behaviors for the absorption and emission cases. Indeed, the cross-section σ_{12} is related to the population levels via

$$\sigma_{12} = -\frac{\boldsymbol{\mu}_{12}^2(N_2 - N_1)}{3\hbar} \tag{8}$$

where μ_{12} is the dipole matrix element, N_1 and N_2 the density of atoms in the ground state and excited states, respectively. For absorption transitions (where $N_2 < N_1$) Eq. 7 describes the usual transition from weak coupling to strong coupling, manifesting itself as vacuum Rabi splitting within the semi-classical framework. As the cross-section becomes negative for emission processes ($N_2 > N_1$), the term $4K_{12}A_m$ in the discriminant of Eq. 7 becomes negative too. For sufficiently large coupling strength g_e the sign flip for an emission line produces a splitting behavior similar to the fork observed in $\mathcal{PT}$-symmetry breaking scenarios. These two distinct behaviors will be described in detail in section 3 where we discuss the results.

In the complete case of four-level dyes, coupling occurs simultaneously to both emission and absorption lines. Each line provides its own polarization P_e and P_a that interacts with

the amplitude E of the optical mode. This results in a modified coupling model:

$$\partial_t \begin{pmatrix} E \\ P_a/\varepsilon_0 \\ P_e/\varepsilon_0 \end{pmatrix} = -i\tilde{\Omega} \begin{pmatrix} E \\ P_a/\varepsilon_0 \\ P_e/\varepsilon_0 \end{pmatrix} = \begin{pmatrix} -i\Omega_m & iA_m & iA_m \\ iK_a & -i\Omega_a & 0 \\ iK_e & 0 & -i\Omega_e \end{pmatrix} \begin{pmatrix} E \\ P_a/\varepsilon_0 \\ P_e/\varepsilon_0 \end{pmatrix} \tag{9}$$

where Ω_a and Ω_e denote the complex frequencies of absorption and emission lines, respectively. The matrix elements $K_{a,e} = \sigma_{a,e}/\varepsilon_0$ are expressed in terms of the cross-sections σ_a and σ_e, which in turn are proportional to the coupling strengths g_a and g_e, respectively. It follows that solving the eigenvalue equation determines the three eigenfrequencies $\tilde{\Omega}$. As $K_a > 0$ and $K_e < 0$, a mixed behavior of Rabi splitting and $\mathcal{PT}$-symmetry breaking is expected for sufficiently large coupling strengths, as discussed next.

3 Results

Having introduced the structure and the semi-analytical theory, we proceed to investigate the active HMM dispersion. Again we first consider the absorption and emission lines in isolation, and later we employ the full four-level dye system. In each part we compare the discrete mode behavior in finite structures with the resulting deformation of bands in infinite structures. The semi-classical model is applied to a specific discrete mode, and provides a good description of the behavior for finite devices in all cases (loss, gain and both). As we will see, the absorption line produces the classical strong coupling behaviour (Rabi splitting), whereas the emission line leads to a fork-like splitting and the appearance of exceptional points.

Absorption: Weak and Strong Coupling. We focus on the effect of an absorption line on the dispersion, ignoring the emission for the moment. Qualitatively we can distinguish two regimes, a weak coupling regime characterized by small distortions of the dispersion, and a strong coupling regime leading to Rabi splitting of modes.

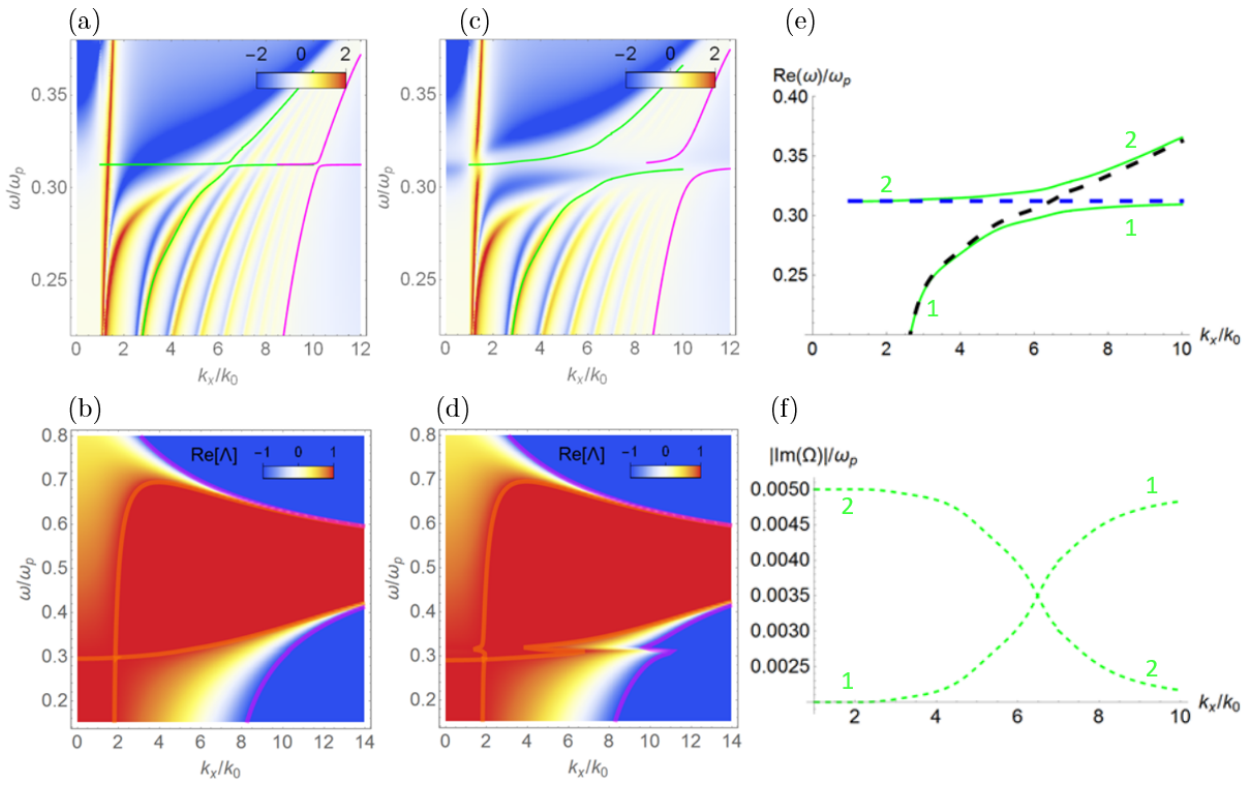

Figure 3: (a) Reflectance with an absorption line in the weak coupling regime ($g_a = 3 \times 10^{12}$) and (c) strong coupling regime ($g_a = 10^{14}$) for the finite structure (logarithmic scale). The green and magenta curves are obtained via our semi-classical model for two different modes. (b) Dispersion diagram of the infinite structure with an absorption line in the weak coupling regime and (d) strong coupling regime. Orange curves are the edges of the plasmonic band at the center of the Brillouin zone ($\mathrm{Re}(\Lambda) = 1$) and magenta curves at the edge of the Brillouin zone ($\mathrm{Re}(\Lambda) = -1$). (e) and (f) real and imaginary parts of the complex eigenfrequencies $\Omega_\pm$ obtained with the model (green curves) in the strong coupling regime. Blue dashed curve is the excitonic absorption line and black dashed curve is the unperturbed optical mode. The two polaritons resulting from the coupling of the optical mode with the excitonic line are identified by the numbers 1 and 2 (Ω_- and Ω_+, respectively).

Figure 3a shows the reflectance map of a 10-period finite structure via transfer-matrix calculations, with each reflectance maximum indicating a discrete plasmonic mode. For a small value of the oscillator coupling strength ($g_a = 3 \times 10^{12}$) a slight perturbation and smearing of the optical modes is observed around $\omega_a = 0.313\,\omega_p$ when compared with the passive case (Figure 2a).

When applying the semi-classical model to two particular modes (green and magenta curves in Figure 3a), one obtains an excellent fit to the exact transfer-matrix results. A

slight deviation from the passive case around ω_a is visible for the green curve e.g., indicating the coupling with the dye. We can understand the weak coupling from the model equations 7, as in this regime $|4K_aA_m| \ll |\Omega_m - \Omega_a|^2$, so $\Omega_+ \approx \Omega_m$ and $\Omega_- \approx \Omega_a$. This means that one mode retains the character of the optical mode, and the other that of the excitonic line.

A similar small perturbation around ω_a is observable at the band edge of the infinite multilayer (Figure 3b) showing the real part of Λ (analytically calculated with Eq. 1). The orange curves correspond to the plasmonic band edge at the center of the Brillouin zone ($\mathrm{Re}(\Lambda) = 1$), while the magenta curve is the plasmonic band edge at the edge of the Brillouin zone ($\mathrm{Re}(\Lambda) = -1$). Comparing the band edges in the active case of Figure 3b (orange and magenta curves) with the band edges in the passive case of Figure 1c (orange and purple curves), one can see that the absorption line causes only a very small deviation.

However, the dispersion qualitatively changes in the strong coupling regime for a larger coupling strength ($g_a = 10^{14}$, Figure 3c), where anti-crossings appear and a gap opens in the reflectance map. This effect is particularly visible for the discrete modes of finite structures, and we plot the same two modes as before using the model with green and magenta curves. Again, the model fits well with the exact results, even in this strongly coupled case. We can understand the behavior by inspection of Eq. 7: close to the crossing point of the optical mode and the excitonic line ($\omega_m = \omega_a$) the first term in the square root dominates and one obtains $(\Omega_m - \Omega_a)^2 \approx (\gamma_m - \gamma_a)^2$. If $\mathrm{Re}(4K_aA_m) \gg (\gamma_m - \gamma_a)^2$ and $\mathrm{Re}(4K_aA_m) \gg \gamma_m, \gamma_a$ (the resonance linewidth of the optical mode and the exciton needs to be smaller than the splitting to be in the strong coupling regime), the square root becomes real and a gap opens. The width of this gap is the Rabi splitting energy $\hbar\Omega_{Rabi} = \sqrt{2K_aA_m}$, with A_m containing the overlap factor Γ. When the order of the optical mode increases, the number of nodes of the mode profile also increases, reducing slightly Γ and thus the Rabi splitting. An analogous situation was reported by Shekhar and Jacob[41], where they studied the interaction between intersubband transitions of multiple quantum well layers and optical modes in a HMM.

Interestingly, our model allows to directly determine the Rabi splitting with only prior

knowledge of the dispersion characteristics of the unperturbed optical mode and the absorption line (Figure 3e). Figure 3e shows the dispersion of the polaritons calculated with our model (green curves) using parameters of the excitonic line (blue dashed curve) and the unperturbed optical mode (black dashed curve). Away from the crossing, the polaritons simply follow the two components, with one polariton being dominantly plasmonic (polariton 1) while the other is dominantly excitonic (polariton 2) for small wavevector k_x (and vice versa for large k_x). At the crossing point a gap opens and the two polaritons are a mixed state between an excitonic and a plasmonic mode.

Another advantage of our model is that we can not only retrieve the real parts of the polaritonic eigenfrequencies, but also their imaginary parts (Figure 3f), thus providing the essential mode characteristics, while most other models convey only the real parts. For example, the imaginary parts of $\Omega_\pm$ are small in the region where we can see the modes in Figure 3c, and large in the more blurry parts where the modes become overdamped. This is the reason why only polariton 1 is visible for small wavevectors k_x (as the imaginary part of the eigenfrequency of polariton 1 increases in magnitude with k_x) and only polariton 2 for large k_x (as the imaginary part of the eigenfrequency of polariton 2 decreases in magnitude with k_x).

The strong coupling effect is also observed in the infinite structure (Figure 3d), where bands arise from the continuum of resonances. In the absence of discrete resonances the impact of strong coupling is less obvious, as the gap effectively closes due to the superposition of an infinite number of dispersive modes. At the band edges however, a strong distortion is observed (analytical calculation of Λ in Figure 3d) around ω_a, which corresponds with the anti-crossings of the finite stack. Indeed, the band edges tend to larger or smaller values of k_x, below or above the absorption line, respectively.

Emission: Exceptional Points. We next consider the emission line in isolation, ignoring the absorption line. For emission processes K_e (via σ_e) changes sign in Eq. 8, and the first term in the square root of Eq. 7 also changes sign. However, for a small coupling

strength (such as $g_e = 3 \times 10^{12}$) one has $|4K_e A_m| \ll |\Omega_m - \Omega_e|^2$, so the situation is similar to a weakly coupled absorption line, where modes become only slightly perturbed (not shown), just as in Figure 3a and 3b.

The situation becomes more interesting for larger coupling strength ($g_e = 10^{14}$) when the linewidths of the optical mode and emission line are similar and small compared to the frequencies, which is true for our parameters ($\gamma_m = 0.004\,\omega_p \approx \gamma_e = 0.005\,\omega_p$). Again we notice from the reflectance map of the finite structure (Figure 4a) that a gap opens for the plasmonic modes around the emission frequency ($\omega_e = 0.288\,\omega_p$). The modes bend towards smaller k_x below the emission line and towards larger k_x above. This behavior is opposite to the previous case where we only took the absorption line into account. With the semi-classical model applied to two particular mode couples (green and magenta lines in Figure 4a), we again obtain a very good agreement with the exact results.

To understand the behavior with the model equations, we examine the argument of the square root of Eq. 7: $\sqrt{4K_e A_m + (\omega_m - \omega_e)^2}$. As the first term becomes large and negative when the coupling strength increases, the square root becomes almost purely complex in the regime where $|4K_e A_m| > [\omega_m(k_x) - \omega_e]^2$, which means that both eigenfrequencies $\Omega_\pm$ have the same real parts but imaginary parts with opposite signs. In other words, this regime is similar to the broken-symmetry phase of $\mathcal{PT}$ systems that produce fork-like bifurcations and give rise to exceptional points when the two modes merge. As a side note we point out that $\mathcal{PT}$-symmetric hypercrystals made of HMMs were studied in[59], but the gain was introduced in the dielectric surrounding the HMM, and not directly into the HMM as proposed here.

To analyze the coupling behaviour in more detail we show the uncoupled and coupled modes in Figure 4c for a particular optical mode (corresponding the the green curve in Figure 4a). The two branches of the fork correspond to the polaritons 1 and 2 in Figure 4c. However, only polariton 2 appears in the reflectance map of Figure 4a. The imaginary part of polariton 1 (not visible in Figure 4a) has a large imaginary part of the eigenfrequency (Figure 4d) and is therefore strongly damped (broadened line), while the polariton 2 has a

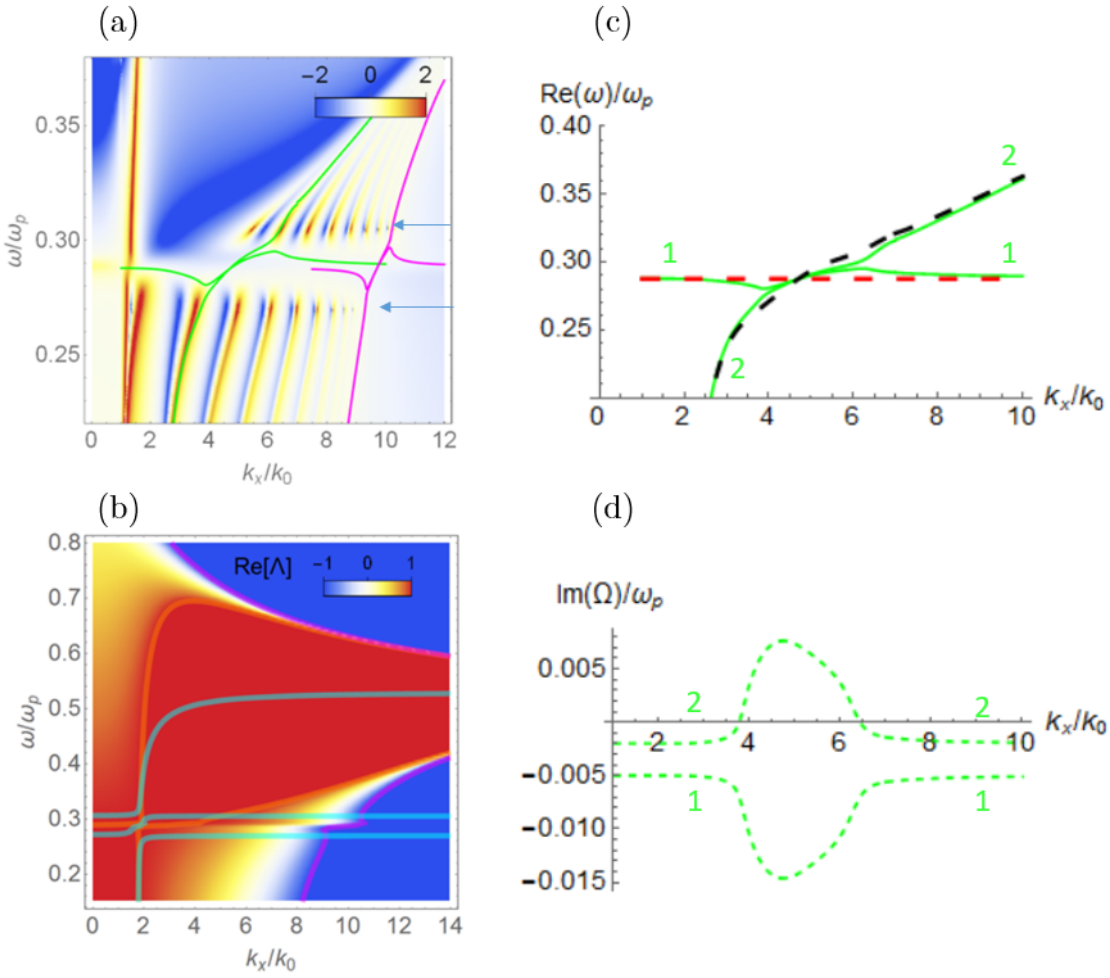

Figure 4: (a) Reflectance with an emission line in the large coupling strength regime ($g_e = 10^{14}$) for the finite structure (logarithmic scale). The green and magenta curves obtained via our semi-classical model on two different modes. (b) Dispersion diagram of the infinite structure with an emission line in the large coupling strength regime. Orange curves are the edges of the plasmonic band at the center of the Brillouin zone ($\mathrm{Re}(\Lambda) = 1$), magenta curves at the edge of the Brillouin zone ($\mathrm{Re}(\Lambda) = -1$) and cyan curves are the loss-compensation boundary ($\mathrm{Im}(\Lambda) = 0$). (c) Real (green solid curves) and (d) imaginary (green dashed curves) parts of the complex eigenfrequencies $\Omega_\pm$ obtained with our semi-classical model. In (c) the red dashed curve is the excitonic emission line and the black dashed curve is the unperturbed optical mode. The two polaritons resulting from the coupling of the optical mode with the excitonic line are identified by the green numbers 1 and 2 (Ω_+ and $\Omega-$, respectively.

smaller imaginary part and can thus be observed in Figure 4a as a sharp resonance, except in the gap region where its imaginary part is positive and large (gain).

The 'lines of points' appearing in the large gain case around $\omega = 0.27\,\omega_p$ and $\omega = 0.31\,\omega_p$ (highlighted by the blue arrows in Figure 4a) are not true exceptional points. Indeed, they

would be 'pure' exceptional points if the square root in equation 7 would be zero (so that the eigenvalues are degenerate), which is not exactly the case here. However, these high-reflection points are regions where the imaginary part of the eigenfrequency of polariton 2 is close to zero (see Figure 4d), and thus the resonances becomes very sharp.

Just as for the absorption case, remnants of the fork-like splitting can be observed only at the edges of the plasmonic band of the infinite multilayer structure (Figure 4b, showing the real part of Λ). An important distortion is observed around $\omega_e = 0.288\,\omega_p$ where the band edges ($\mathrm{Re}(\Lambda) = +1$, orange curves, and $\mathrm{Re}(\Lambda) = -1$, magenta curves) undergo a distortion similar to the one of the resonances of the finite stack. Indeed, the band edges tend to smaller (larger) k_x below (above) the emission line. The cyan curves in Figure 4b are the loss-gain compensation boundaries ($\mathrm{Im}(\Lambda) = 0$), which intersect the band edges. From equation 2 we know that here the condition for the generation of exceptional points is met. True exceptional points thus appear in the case of an infinite multilayer, as discussed in more detail in the next section.

Strong Gain-Loss Interaction. We introduce the full four-level dispersion of pumped dye molecules, including both the absorption and emission line. We will see that loss compensation and the appearance of exceptional points are directly connected.

Figure 5a shows the reflectance map obtained with the transfer-matrix method of the finite structure for large coupling strengths $g = g_a = g_e = 10^{14}$. As before, the maxima of reflectance are discrete modes, and we apply the full semi-classical model Eq. 9 for two optical modes (green and magenta) to obtain the polaritons. Zoom-ins on the splitting behaviour with the model are provided by Figures 5c and 5d.

The blurry regions (around 0.28-0.29 ω_p and 0.31-0.32 ω_p) occur when the magnitude of the imaginary part of the eigenfrequencies becomes large, while regions where discrete modes are visible have very small imaginary parts (Figure 5d). At the absorption line (blue curve in Figure 5c) the typical mode-splitting occurs, while at the emission line (red curve in Figure 5c) the fork-like features of $\mathcal{PT}$ systems are present (Figure 5c). In the region

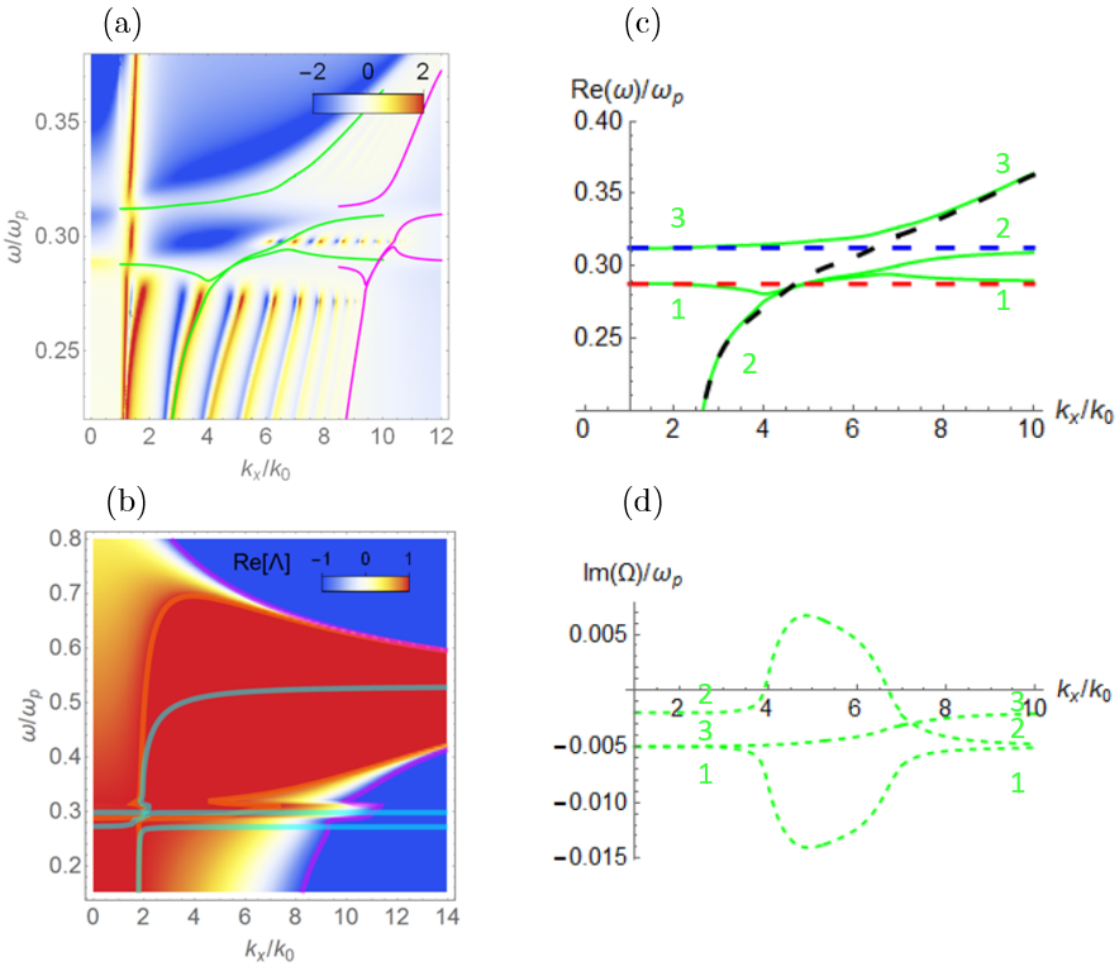

Figure 5: (a) Reflectance with both absorption and emission in the large coupling strength regime ($g = 10^{14}$) for the finite structure (logarithmic scale). The green and magenta curves are obtained via our semi-classical model on two different modes. (b) Dispersion diagram of the infinite structure with both absorption and emission lines in the large coupling strength regime. Orange curves are the edges of the plasmonic band at the center of the Brillouin zone ($\mathrm{Re}(\Lambda) = 1$), magenta curves at the edge of the Brillouin zone ($\mathrm{Re}(\Lambda) = -1$) and cyan curves are the loss-compensation boundary ($\mathrm{Im}(\Lambda) = 0$). (c) Real (green solid curves) and (d) imaginary (green dashed curves) parts of the complex eigenfrequencies $\tilde{\Omega}$ obtained with our semi-classical model. In (c) the red dashed curve is the excitonic emission line, the blue dashed curve is the excitonic absorption line and the black dashed curve is the unperturbed optical mode. The three polaritons resulting from the coupling of the optical mode with the two excitonic lines are identified by the green numbers 1, 2 and 3.

between the two excitonic lines (between ω_e and ω_a) the modes tend towards large k_x and can reach extremely high values of the effective index (for example, the bifurcation point of the green mode around $\omega = 0.3\,\omega_p$ in Figure 5c has an effective index of 7, while at this

frequency the effective index was 4 in the passive HMM). Only the dispersion of polaritons 3 and 2 (for small k_x and in the vicinity of the gain/loss compensation points) can be observed in Figure 5a, because of their small (in magnitude) imaginary parts of their eigenfrequencies. Polariton 1 cannot be observed as it is always overdamped (Figure 5d).

As discussed previously, the emission and absorption lines exert a similar effect on the band edges of the infinite HMM. In this case the forks at the edges provide real EPs, unlike the points in the dispersion diagram of the finite structure where a vanishing imaginary part produces just lines of sharp resonances. In Figure 5b (the real part of Λ of the infinite HMM) an important distortion is observed around ω_e and ω_a, where the band edges ($\mathrm{Re}(\Lambda) = +1$, orange curves, and $\mathrm{Re}(\Lambda) = -1$, magenta curves) undergo a distortion similar to the resonances of the finite stack. The cyan curves in Figure 5b are the loss-gain compensation boundaries, which intersect the band edges. At these intersections $\Lambda = \pm 1$, so from equation 2 one concludes that the eigenvalues are degenerate, and that these points are thus EPs.

The presence of EPs has significant implications in the infinite structure, e.g. on the group index (along z) $n_{g,z}$ (calculated using the implicit function theorem[60]), see Figure 6a. Five EPs exist with the chosen parameters. Zoom-ins on two EPs (EP1 and EP2, one on each band edge) are also shown in Figures 6b and 6c, providing evidence that $n_{g,z}$ diverges, which is a signature of the existence of exceptional points, connecting with recent results in[61]. These singularities were also studied recently by Pick *et al.*[62].

Note that there is a very direct connection in position (in the (k_x, ω) dispersion coordinates) between the EPs of the infinite and the finite multilayer. For the finite structure one compares with the two 'lines of points' in Figure 5a ($\omega = 0.275\,\omega_p$ and $\omega = 0.3\,\omega_p$), but only with the points at the smallest and largest k_x for each line. For instance, EP1 is visible in both Figure 6a and Figure 5a at $\omega = 0.275\,\omega_p$ and $k_x/k_0 = 9$. Similarly, EP3 is both times visible at $\omega = 0.3\,\omega_p$ and $k_x/k_0 = 6$. This correspondence shows that in both cases the exceptional points arise effectively from a mechanism similar to $\mathcal{PT}$-symmetry.

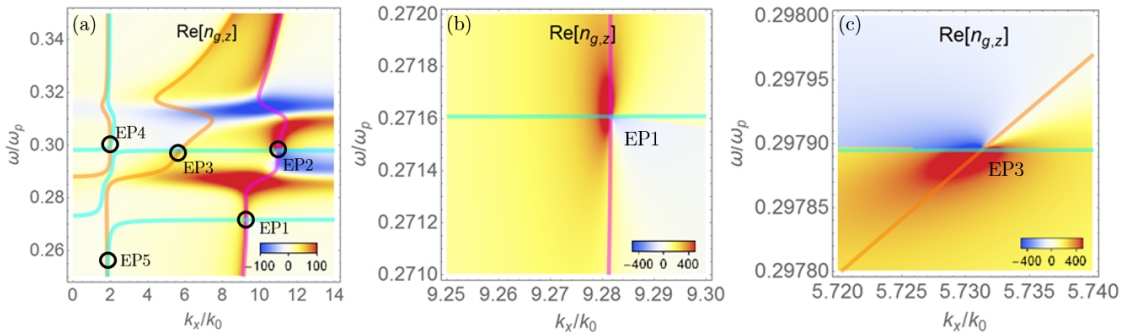

Figure 6: (a) Group index in z direction $n_{g,z}$ of the dye infiltrated multilayer. (b) Zoom on EP1. (c) Zoom on EP3. Orange curves correspond to the band edges at the Brillouin zone center $k_z D = 0$, magenta curves correspond to the the band edges at the Brillouin zone edge $k_z D = \pi$, and cyan curves correspond to the gain-loss compensation line where $\mathrm{Im}(\Lambda) = 0$.

Conclusion

Introduction of gain in HMMs provides a means for loss-compensation and opens a convenient route facilitating injection of light into hyperbolic modes, which are otherwise not directly accessible from within the light cone. In this paper we have studied the impact of four-level dye molecules embedded in the dielectric medium of multilayer HMMs. We considered both the weak and strong coupling regime of interaction with the emission and absorption lines, respectively. We developed a semi-analytical model to describe these phenomena and demonstrated that the model fits very well with the exact results obtained by the transfer-matrix method. In the weak coupling regime we observe, as expected, only a small perturbation of the band without apparent differences. In the strong coupling regime, however, both emission and absorption lines produce extreme distortions of the plasmonic band due to Rabi splitting and a $\mathcal{PT}$-symmetry broken phase with generation of EPs at the loss-gain compensation frequencies. These results are important for active components with HMMs, and for the use of EPs in active multilayers.

Acknowledgement

This work is supported by the Belgian Science Policy Office under the project 'Photonics@be' (P7-35), and by the Fonds pour la Formation à la Recherche dans l'Industrie et dans l'Agriculture (FRIA) in Belgium.

Supporting Information Available

Semi-classical model for optical mode coupling in 1D periodic structure with excitonic transition. This material is available free of charge via the Internet at http://pubs.acs.org/.

References

(1) W. Cai, V. S. In *Optical Metamaterials: Fundamentals and Applications*; Springer,, Ed.; Springer, 2010.

(2) Skorobogatiy, M. *Nanostructured and Subwavelength Waveguides*; John Wiley & Sons, Ltd, 2012.

(3) Kildishev, A. V.; Boltasseva, A.; Shalaev, V. M. Planar Photonics with Metasurfaces. *Science* **2013**, *339*, 1232009.

(4) Soukoulis, C. M.; Wegener, M. Past achievements and future challenges in the development of three-dimensional photonic metamaterials. *Nat. Photonics* **2011**, *5*, 523–530.

(5) Wurtz, G. A.; Pollard, R.; Hendren, W.; Wiederrecht, G. P.; Gosztola, D. J.; Podolskiy, V. A.; Zayats, A. V. Designed ultrafast optical nonlinearity in a plasmonic nanorod metamaterial enhanced by nonlocality. *Nat. Nanotechnol.* **2011**, *6*, 107–111.

(6) Shadrivov, I. V.; Zharov, A. A.; Kivshar, Y. S. Second-harmonic generation in nonlinear left-handed metamaterials. *J. Opt. Soc. Am. B* **2006**, *23*, 529–534.

(7) Lu, D.; Kan, J. J.; Fullerton, E. E.; Liu, Z. Enhancing spontaneous emission rates of molecules using nanopatterned multilayer hyperbolic metamaterials. *Nat. Nanotechnol.* **2014**, *9*, 48–53.

(8) Galfsky, T.; Krishnamoorthy, H. N. S.; Newman, W.; Narimanov, E. E.; Jacob, Z.; Menon, V. M. Active hyperbolic metamaterials: enhanced spontaneous emission and light extraction. *Optica* **2015**, *2*, 62–65.

(9) Poddubny, A.; Iorsh, I.; Belov, P.; Kivshar, Y. Hyperbolic metamaterials. *Nat. Photonics* **2013**, *7*, 948–957.

(10) Yang, X.; Yao, J.; Rho, J.; Yin, X.; Zhang, X. Experimental realization of three-dimensional indefinite cavities at the nanoscale with anomalous scaling laws. *Nat. Photonics* **2012**, *6*, 450–454.

(11) Sreekanth, K. V.; De Luca, A.; Strangi, G. Experimental demonstration of surface and bulk plasmon polaritons in hypergratings. *Sci. Rep.* **2013**, *3*, 3291.

(12) Krishna, K. H.; Sreekanth, K. V.; Strangi, G. Dye-embedded and nanopatterned hyperbolic metamaterials for spontaneous emission rate enhancement. *J. Opt. Soc. Am. B* **2016**, *33*, 1038–1043.

(13) Pawlik, G.; Tarnowski, K.; Walasik, W.; Mitus, A. C.; Khoo, I. C. Liquid crystal hyperbolic metamaterial for wide-angle negative-positive refraction and reflection. *Opt. Lett.* **2014**, *39*, 1744–1747.

(14) Krishnamoorthy, H. N. S.; Jacob, Z.; Narimanov, E.; Kretzschmar, I.; Menon, V. M. Topological Transitions in Metamaterials. *Science* **2012**, *336*, 205–209.

(15) Narimanov, E. E.; Li, H.; Barnakov, Y. A.; Tumkur, T. U.; Noginov, M. A. Reduced reflection from roughened hyperbolic metamaterial. *Opt. Express* **2013**, *21*, 14956–14961.

(16) Cortes, C. L.; Newman, W.; Molesky, S.; Jacob, Z. Quantum nanophotonics using hyperbolic metamaterials. *J. Opt* **2012**, *14*, 063001.

(17) Vaianella, F.; Maes, B. Describing the dispersion of plasmonic nanorod arrays via coupling of elementary excitations. *Phys. Rev. B* **2016**, *93*, 165417.

(18) Wood, B.; Pendry, J. B.; Tsai, D. P. Directed subwavelength imaging using a layered metal-dielectric system. *Phys. Rev. B* **2006**, *74*, 115116.

(19) Casse, B. D. F.; Lu, W. T.; Huang, Y. J.; Gultepe, E.; L., M.; Sridhar, S. Super-resolution imaging using a three-dimensional metamaterials nanolens. *Appl. Phys. Lett.* **2010**, *96*, 023114.

(20) Xiong, Y.; Liu, Z.; Zhang, X. A simple design of flat hyperlens for lithography and imaging with half-pitch resolution down to 20 nm. *Appl. Phys. Lett.* **2009**, *94*, 203108.

(21) Xiong, Y.; Liu, Z.; Zhang, X. Projecting deep-subwavelength patterns from diffraction-limited masks using metal-dielectric multilayers. *Appl. Phys. Lett.* **2008**, *93*, 111116.

(22) Vaianella, F.; Maes, B. Fano resonance engineering in slanted cavities with hyperbolic metamaterials. *Phys. Rev. B* **2016**, *94*, 125442.

(23) Andryieuski, A.; Zhukovsky, S. V.; Lavrinenko, A. V. Rough metal and dielectric layers make an even better hyperbolic metamaterial absorber. *Opt. Express* **2014**, *22*, 14975–14980.

(24) Nefedov, I. S.; Valagiannopoulos, C. A.; Hashemi, S. M.; Nefedov, E. I. Total absorption in asymmetric hyperbolic media. *Sci. Rep.* **2013**, *3*, 2662.

(25) Guclu, C.; Campione, S.; Capolino, F. Hyperbolic metamaterial as super absorber for scattered fields generated at its surface. *Phys. Rev. B* **2012**, *86*, 205130.

(26) Hess, O.; Pendry, J. B.; Maier, S. A.; Oulton, R. F.; Hamm, J. M.; Tsakmakidis, K. L. Active nanoplasmonic metamaterials. *Nat. Mater.* **2012**, *11*, 573–584.

(27) Wuestner, S.; Pusch, A.; Tsakmakidis, K. L.; Hamm, J. M.; Hess, O. Overcoming Losses with Gain in a Negative Refractive Index Metamaterial. *Phys. Rev. Lett.* **2010**, *105*, 127401.

(28) Meinzer, N.; Ruther, M.; Linden, S.; Soukoulis, C. M.; Khitrova, G.; Hendrickson, J.; Olitzky, J. D.; Gibbs, H. M.; Wegener, M. Arrays of Ag split-ring resonators coupled to InGaAs single-quantum-well gain. *Opt. Express* **2010**, *18*, 24140–24151.

(29) Noginov, M. A.; Zhu, G.; Belgrave, A. M.; Bakker, R.; Shalaev, V. M.; Narimanov, E. E.; Stout, S.; Herz, E.; Suteewong, T.; Wiesner, U. Demonstration of a spaser-based nanolaser. *Nature* **2009**, *460*, 1110–1113.

(30) Noginov, M. A.; Zhu, G.; Bahoura, M.; Adegoke, J.; Small, C. E.; Ritzo, B. A.; Drachev, V. P.; Shalaev, V. M. Enhancement of surface plasmons in an Ag aggregate by optical gain in a dielectric medium. *Opt. Lett.* **2006**, *31*, 3022–3024.

(31) Xiao, S.; Drachev, V. P.; Kildishev, A. V.; Ni, X.; Chettiar, U. K.; Yuan, H.-K.; Shalaev, V. M. Loss-free and active optical negative-index metamaterials. *Nature* **2010**, *466*, 735–740.

(32) Fang, A.; Koschny, T.; Wegener, M.; Soukoulis, C. M. Self-consistent calculation of metamaterials with gain. *Phys. Rev. B* **2009**, *79*, 241104.

(33) Argyropoulos, C.; Estakhri, N. M.; Monticone, F.; Alù, A. Negative refraction, gain and nonlinear effects in hyperbolic metamaterials. *Opt. Express* **2013**, *21*, 15037–15047.

(34) Wan, M.; Gu, P.; Liu, W.; Chen, Z.; Wang, Z. Low threshold spaser based on deep-subwavelength spherical hyperbolic metamaterial cavities. *Appl. Phys. Lett.* **2017**, *110*, 031103.

(35) Smalley, J. S. T.; Vallini, F.; Kant?, B.; Fainman, Y. Modal amplification in active

waveguides with hyperbolic dispersion at telecommunication frequencies. *Opt. Express* **2014**, *22*, 21088–21105.

(36) Janaszek, B.; Tyszka-Zawadzka, A.; Szczepanski, P. Control of gain/absorption in tunable hyperbolic metamaterials. *Opt. Express* **2017**, *25*, 13153–13162.

(37) Ni, X.; Ishii, S.; Thoreson, M. D.; Shalaev, V. M.; Han, S.; Lee, S.; Kildishev, A. V. Loss-compensated and active hyperbolic metamaterials. *Opt. Express* **2011**, *19*, 25242–25254.

(38) Rodriguez, S. R.-K. Classical and quantum distinctions between weak and strong coupling. *Eur. J. Phys.* **2016**, *37*, 025802.

(39) Li, R.-Q.; Garcia-Vidal, F. J.; Fernandez-Dominguez, A. I. Plasmon-Exciton Coupling in Symmetry-Broken Nanocavities. *ACS Photonics* **2018**, *5*, 177–185.

(40) Feist, J.; Galego, J.; Garcia-Vidal, F. J. Polaritonic Chemistry with Organic Molecules. *ACS Photonics* **2018**, *5*, 205–216.

(41) Shekhar, P.; Jacob, Z. Strong coupling in hyperbolic metamaterials. *Phys. Rev. B* **2014**, *90*, 045313.

(42) Lupu, A.; Benisty, H.; Degiron, A. Switching using PT symmetry in plasmonic systems: positive role of the losses. *Opt. Express* **2013**, *21*, 21651–21668.

(43) Phang, S.; Vukovic, A.; Creagh, S. C.; Sewell, P. D.; Gradoni, G.; Benson, T. M. Localized Single Frequency Lasing States in a Finite Parity-Time Symmetric Resonator Chain. *Sci. Rep.* **2016**, *6*, 20499.

(44) Zayats, A. V.; Maier, S. A. *Active Plasmonics and Tuneable Plasmonic Metamaterials*; John Wiley & Sons, 2013.

(45) Zhukovsky, S. V.; Kidwai, O.; Sipe, J. E. Physical nature of volume plasmon polaritons in hyperbolic metamaterials. *Opt. Express* **2013**, *21*, 14982–14987.

(46) Zhukovsky, S. V.; Andryieuski, A.; Sipe, J. E.; Lavrinenko, A. V. From surface to volume plasmons in hyperbolic metamaterials: General existence conditions for bulk high-k waves in metal-dielectric and graphene-dielectric multilayers. *Phys. Rev. B* **2014**, *90*, 155429.

(47) Narimanov, E. E. Photonic Hypercrystals. *Phys. Rev. X* **2014**, *4*, 041014.

(48) Ferrari, L.; Wu, C.; Lepage, D.; Zhang, X.; Liu, Z. Hyperbolic metamaterials and their applications. *Prog. Quantum Electron.* **2015**, *40*, 1–40.

(49) Orlov, A. A.; Voroshilov, P. M.; Belov, P. A.; Kivshar, Y. S. Engineered optical nonlocality in nanostructured metamaterials. *Phys. Rev. B* **2011**, *84*, 045424.

(50) Iorsh, I.; Poddubny, A.; Orlov, A.; Belov, P.; Kivshar, Y. S. Spontaneous emission enhancement in metal-dielectric metamaterials. *Phys. Lett. A* **2012**, *376*, 185–187.

(51) Rosenblatt, G.; Orenstein, M. Competing coupled gaps and slabs for plasmonic metamaterial analysis. *Opt. Express* **2011**, *19*, 20372–20385.

(52) Zhukovsky, S. V.; Orlov, A. A.; Babicheva, V. E.; Lavrinenko, A. V.; Sipe, J. E. Photonic-band-gap engineering for volume plasmon polaritons in multiscale multilayer hyperbolic metamaterials. *Phys. Rev. A* **2014**, *90*, 013801.

(53) Johnson, P. B.; Christy, R. W. Optical Constants of the Noble Metals. *Phys. Rev. B* **1972**, *6*, 4370–4379.

(54) Tassin, P.; Koschny, T.; Kafesaki, M.; Soukoulis, C. M. A comparison of graphene, superconductors and metals as conductors for metamaterials and plasmonics. *Nat. Photonics* **2012**, *6*, 259–264.

(55) Dastmalchi, B.; Tassin, P.; Koschny, T.; Soukoulis, C. M. A New Perspective on Plasmonics: Confinement and Propagation Length of Surface Plasmons for Different Materials and Geometries. *Adv. Opt. Mater.* **2016**, *4*, 177–184.

(56) Kitur, J. K.; Zhu, G.; Barnakov, Y. A.; Noginov, M. A. Stimulated emission of surface plasmon polaritons on smooth and corrugated silver surfaces. *J. Opt.* **2012**, *14*, 114015.

(57) Noginov, M. A.; Podolskiy, V. A.; Zhu, G.; Mayy, M.; Bahoura, M.; Adegoke, J. A.; Ritzo, B. A.; Reynolds, K. Compensation of loss in propagating surface plasmon polariton by gain in adjacent dielectric medium. *Opt. Express* **2008**, *16*, 1385–1392.

(58) Chen, W.; Thoreson, M. D.; Ishii, S.; Kildishev, A. V.; Shalaev, V. M. Ultra-thin ultra-smooth and low-loss silver films on a germanium wetting layer. *Opt. Express* **2010**, *18*, 5124–5134.

(59) Shramkova, O. V.; Tsironis, G. P. Propagation of electromagnetic waves in *PT*-symmetric hyperbolic structures. *Phys. Rev. B* **2016**, *94*, 035141–.

(60) Novotny, O.; Mufti, I.; Vicentini, A. G. Analytical partial derivatives of the phase- and group velocities for Rayleigh waves propagating in a layer on a half-space. *Stud. Geophys. Geod.* **2005**, *49*, 305–321.

(61) Goldzak, T.; Mailybaev, A. A.; Moiseyev, N. Light Stops at Exceptional Points. *Phys. Rev. Lett.* **2018**, *120*, 013901.

(62) Pick, A.; Zhen, B.; Miller, O. D.; Hsu, C. W.; Hernandez, F.; Rodriguez, A. W.; Soljačić, M.; Johnson, S. G. General theory of spontaneous emission near exceptional points. *Opt. Express* **2017**, *25*, 12325–12348.

Graphical TOC Entry